



The TESS–Keck Survey. I. A Warm Sub-Saturn-mass Planet and a Caution about Stray Light in TESS Cameras*

Paul A. Dalba^{1,40} , Arvind F. Gupta^{2,3} , Joseph E. Rodriguez⁴ , Diana Dragomir⁵ , Chelsea X. Huang^{6,41} , Stephen R. Kane¹ , Samuel N. Quinn⁴ , Allyson Bieryla⁴ , Gilbert A. Esquerdo⁴ , Benjamin J. Fulton⁷ , Nicholas Scarsdale⁸ , Natalie M. Batalha⁸ , Corey Beard⁹ , Aida Behmard^{10,42} , Ashley Chontos^{11,42} , Ian J. M. Crossfield¹² , Courtney D. Dressing¹³ , Steven Giacalone¹³ , Michelle L. Hill¹ , Lea A. Hirsch¹⁴ , Andrew W. Howard¹⁵ , Daniel Huber¹¹ , Howard Isaacson^{13,16} , Molly Kosiarek^{8,42} , Jack Lubin⁹ , Andrew W. Mayo^{13,17} , Teo Mocnik¹⁸ , Joseph M. Akana Murphy^{8,43} , Erik A. Petigura¹⁹ , Paul Robertson⁹ , Lee J. Rosenthal¹⁵ , Arpita Roy¹⁵ , Ryan A. Rubenzahl^{15,42} , Judah Van Zandt¹⁹ , Lauren M. Weiss¹¹ , Emil Knudstrup²⁰ , Mads F. Andersen²⁰ , Frank Grundahl²⁰ , Xinyu Yao²¹ , Joshua Pepper²¹ , Steven Villanueva, Jr.^{6,41} , David R. Ciardi⁷ , Ryan Cloutier⁴ , Thomas Lee Jacobs^{22,44} , Martti H. Kristiansen^{23,24} , Darryl M. LaCourse^{25,44} , Monika Lendl^{26,27} , Hugh P. Osborn^{6,28} , Enric Palle²⁹ , Keivan G. Stassun^{30,31} , Daniel J. Stevens^{2,3,45} , George R. Ricker⁶ , Roland Vanderspek⁶ , David W. Latham⁴ , S. Seager^{6,32,33} , Joshua N. Winn³⁴ , Jon M. Jenkins³⁵ , Douglas A. Caldwell^{35,36} , Tansu Daylan^{6,46} , William Fong⁶ , Robert F. Goeke⁶ , Mark E. Rose³⁵ , Pamela Rowden³⁷ , Joshua E. Schlieder³⁸ , Jeffrey C. Smith^{35,36} , and Andrew Vanderburg^{39,47} 

¹ Department of Earth & Planetary Sciences, University of California Riverside, 900 University Ave, Riverside, CA 92521, USA; pdalba@ucr.edu

² Department of Astronomy & Astrophysics, 525 Davey Laboratory, The Pennsylvania State University, University Park, PA, 16802, USA

³ Center for Exoplanets & Habitable Worlds, 525 Davey Laboratory, The Pennsylvania State University, University Park, PA, 16802, USA

⁴ Center for Astrophysics | Harvard & Smithsonian, 60 Garden St, Cambridge, MA 02138, USA

⁵ Department of Physics & Astronomy, University of New Mexico, 1919 Lomas Blvd NE, Albuquerque, NM 87131, USA

⁶ Department of Physics and Kavli Institute for Astrophysics and Space Research, Massachusetts Institute of Technology, Cambridge, MA 02139, USA

⁷ NASA Exoplanet Science Institute, Caltech/IPAC, Pasadena, CA 91125, USA

⁸ Department of Astronomy & Astrophysics, University of California, Santa Cruz, CA 95064, USA

⁹ Department of Physics & Astronomy, The University of California, Irvine, 4129 Frederick Reines Hall, Irvine, CA 92697, USA

¹⁰ Division of Geological & Planetary Science, California Institute of Technology, 1200 E California Blvd, Pasadena, CA 91125, USA

¹¹ Institute for Astronomy, University of Hawai‘i, 2680 Woodlawn Drive, Honolulu, HI 96822, USA

¹² Department of Physics & Astronomy, University of Kansas, Lawrence, KS, USA

¹³ Department of Astronomy, University of California Berkeley, Berkeley, CA 94720-3411, USA

¹⁴ Kavli Institute for Particle Astrophysics and Cosmology, Stanford University, Stanford, CA 94305, USA

¹⁵ Department of Astronomy, California Institute of Technology, 1200 E California Blvd, Pasadena, CA 91125, USA

¹⁶ University of Southern Queensland, Toowoomba, QLD 4350, Australia

¹⁷ Centre for Star & Planet Formation, Natural History Museum of Denmark & Niels Bohr Institute, University of Copenhagen, Øster Voldgade 5-7, DK-1350 Copenhagen K, Denmark

¹⁸ Gemini Observatory Northern Operations, 670 N. A‘hoku Place, Hilo, HI 96720, USA

¹⁹ Department of Physics & Astronomy, University of California Los Angeles, Los Angeles, CA 90095, USA

²⁰ Stellar Astrophysics Centre, Department of Physics and Astronomy, Aarhus University, Ny Munkegade 120, DK-8000 Aarhus C, Denmark

²¹ Department of Physics, Lehigh University, 16 Memorial Drive East, Bethlehem, PA 18015, USA

²² 12812 SE 69th Place, Bellevue, WA 98006, USA

²³ DTU Space, National Space Institute, Technical University of Denmark, Elektrovej 327, DK-2800 Lyngby, Denmark

²⁴ Brorfelde Observatory, Observator Gyldenkernes Vej 7, DK-4340 Tølløse, Denmark

²⁵ 7507 52nd Pl NE, Marysville, WA 98270, USA

²⁶ Observatoire de Genève, Université de Genève, 51 Ch. des Maillettes, 1290 Sauverny, Switzerland

²⁷ Space Research Institute, Austrian Academy of Sciences, Schmiedlstr. 6, A-8042 Graz, Austria

²⁸ Center for Space and Habitability, University of Bern, Gesellschaftsstrasse 6, CH-3012 Bern, Switzerland

²⁹ Instituto de Astrofísica de Canarias (IAC), E-38200 La Laguna, Tenerife, Spain

³⁰ Vanderbilt University, Department of Physics & Astronomy, 6301 Stevenson Center Ln., Nashville, TN 37235, USA

³¹ Fisk University, Department of Physics, 1000 18th Ave. N., Nashville, TN 37208, USA

³² Department of Earth, Atmospheric and Planetary Sciences, Massachusetts Institute of Technology, Cambridge, MA 02139, USA

³³ Department of Aeronautics and Astronautics, MIT, 77 Massachusetts Avenue, Cambridge, MA 02139, USA

³⁴ Department of Astrophysical Sciences, Princeton University, 4 Ivy Lane, Princeton, NJ 08544, USA

³⁵ NASA Ames Research Center, Moffett Field, CA 94035, USA

³⁶ SETI Institute, Mountain View, CA 94043, USA

³⁷ School of Physical Sciences, The Open University, Milton Keynes MK7 6AA, UK

³⁸ Exoplanets and Stellar Astrophysics Laboratory, Mail Code 667, NASA Goddard Space Flight Center, Greenbelt, MD 20771, USA

* Some of the data presented herein were obtained at the W. M. Keck Observatory, which is operated as a scientific partnership among the California Institute of Technology, the University of California and the National Aeronautics and Space Administration. The Observatory was made possible by the generous financial support of the W. M. Keck Foundation.

³⁹Department of Astronomy, The University of Texas at Austin, Austin, TX 78712, USA
 Received 2020 January 16; revised 2020 March 20; accepted 2020 March 27; published 2020 April 29

Abstract

We report the detection of a Saturn-size exoplanet orbiting HD 332231 (TOI 1456) in light curves from the Transiting Exoplanet Survey Satellite (TESS). HD 332231—an F8 dwarf star with a V -band magnitude of 8.56—was observed by TESS in Sectors 14 and 15. We detect a single-transit event in the Sector 15 presearch data conditioning (PDC) light curve. We obtain spectroscopic follow-up observations of HD 332231 with the Automated Planet Finder, Keck I, and SONG telescopes. The orbital period we infer from radial velocity (RV) observations leads to the discovery of another transit in Sector 14 that was masked by PDC due to scattered light contamination. A joint analysis of the transit and RV data confirms the planetary nature of HD 332231 b, a Saturn-size ($0.867^{+0.027}_{-0.025} R_J$), sub-Saturn-mass ($0.244 \pm 0.021 M_J$) exoplanet on a 18.71 day circular orbit. The low surface gravity of HD 332231 b and the relatively low stellar flux it receives make it a compelling target for transmission spectroscopy. Also, the stellar obliquity is likely measurable via the Rossiter–McLaughlin effect, an exciting prospect given the 0.14 au orbital separation of HD 332231 b. The spectroscopic observations do not provide substantial evidence for any additional planets in the HD 332231 system, but continued RV monitoring is needed to further characterize this system. We also predict that the frequency and duration of masked data in the PDC light curves for TESS Sectors 14–16 could hide transits of some exoplanets with orbital periods between 10.5 and 17.5 days.

Unified Astronomy Thesaurus concepts: Exoplanet astronomy (486); Radial velocity (1332); Transit photometry (1709); Exoplanet detection methods (489); Exoplanets (498); F dwarf stars (516); Spectroscopy (1558); Direct imaging (387)

Supporting material: machine-readable table

1. Introduction

NASA’s Transiting Exoplanet Survey Satellite (TESS) has already led to the discovery of nearly three dozen planets announced in papers that have been submitted or published. Thousands more are expected, and we are well on our way toward this plethora of planets, as evidenced by the over one thousand planet candidate TESS Objects of Interest (TOIs) already found (N. Guerrero et al. 2020, in preparation). Much of the follow-up effort has been focused on confirming and characterizing the small planets (e.g., Huang et al. 2018; Dragomir et al. 2019; Vanderburg et al. 2019; Winters et al. 2019). Several giant exoplanets have been confirmed as well (e.g., Huber et al. 2019; Jones et al. 2019; Rodriguez et al. 2019; Wang et al. 2019). However, due to observational biases, the TESS primary mission strategy, and the ease of characterizing planets that transit frequently, most of the TESS planets announced to date orbit relatively close to their stars.

Yet the “bright star advantage” of TESS can also apply to longer-period exoplanets (e.g., Eisner et al. 2019). Only a few dozen exoplanets with orbital periods greater than 15 days and precisely measured radii and radial velocity (RV) determined masses are currently known.⁴⁸ Of these, only six orbit stars with V -band magnitude brighter than 10. This deficiency has impeded robust tests of the theories surrounding planetary interiors and formation. For example, Jupiter and Saturn are

often included on exoplanet mass–radius relations where the Jovian regime is largely informed by hot Jupiters (e.g., Chen & Kipping 2017). A more informative comparison could be made to cooler exoplanets that have not experienced dramatically different evolutionary histories.

TESS has the potential to reveal hundreds of new, weakly irradiated planets transiting bright stars, but many of them will show just one transit during the primary mission (Sullivan et al. 2015; Cooke et al. 2018; Gill et al. 2019; Lendl et al. 2020; Villanueva et al. 2019, e.g.). In this paper, we present HD 332231 b, a transiting warm sub-Saturn-mass planet initially discovered as a single-transit planet candidate through the TOI identification and vetting process described in detail in a separate paper (N. Guerrero et al. 2020, in preparation). Briefly, TOIs are identified in the TESS short-cadence “postage stamp” light curves with the Transit Planet Search tool (Twicken et al. 2016) or in the long-cadence full-frame image light curves using the Box Least Squares algorithm (Kovács et al. 2002). TOIs are then vetted through the use of several diagnostics such as an odd–even transit depth test, a weak secondary eclipse test, a difference image centroid test, and examination of the light curves obtained with multiple apertures. After the TESS discovery of HD 332231 b, an RV follow-up campaign ensued, uncovering a likely orbital period of ~ 18 days. Since TESS observed HD 332231 in Sectors 14 and 15, this period would mean that at least one other transit should have been caught. Upon closer investigation, another transit (matching the RV period) was indeed discovered in a section of the TESS light curve that had been masked out prior to the TOI search due to contamination by scattered light. This sequence of events mirrors that described by Dragomir et al. (2019) and Eisner et al. (2019) regarding spacecraft reaction wheel desaturation events (i.e., momentum dumps).

We present the photometric, imaging, and spectroscopic observations of HD 332231 in Section 2. We detail the joint analysis of the TESS light curves and RV observations from

⁴⁰ NSF Astronomy & Astrophysics Postdoctoral Fellow.

⁴¹ Juan Carlos Torres Fellow.

⁴² NSF Graduate Research Fellow.

⁴³ NSF Graduate Research Fellow, LSSTC Data Science Fellow.

⁴⁴ Amateur Astronomer.

⁴⁵ Eberly Fellow.

⁴⁶ Kavli Fellow.

⁴⁷ NASA Sagan Fellow.

⁴⁸ According to the NASA Exoplanet Archive <https://exoplanetarchive.ipac.caltech.edu/>.

multiple observatories in Section 3. Section 4 contains a discussion of our results, atmospheric characterization prospects, and the possibility of additional companions in the system. In the same Section, we also carry out an investigation into the number of transits potentially occurring during Sectors 14, 15, and 16 light-curve portions that were affected by scattered light. We conclude in Section 5.

2. Observations

Light curves from TESS gave the first indication of a planet candidate orbiting HD 332231. Following this discovery, we acquired reconnaissance spectra, speckle imaging, and Doppler spectra to further characterize the nature of the system. The following sections describe these observations and the initial analysis we conducted as these data were collected. When a planet candidate is identified through a limited number of transits—only one in this case—the interaction between detection, transit modeling, and RV monitoring is critical for narrowing the parameter space of the system’s properties. We will describe how rapid RV follow-up refined the orbital period of the planet candidate, thereby revealing the existence of a previously missed transit. These steps drastically reduced the amount of time and resources required to characterize the entire system.

2.1. TESS Photometry

TESS observed HD 332231 (also known as TIC 199376584 and TOI 1456) in Sectors 14 and 15 with two-minute cadence. Version 4.0 of the Science Processing Operations Center (SPOC) data pipeline (Jenkins et al. 2016) processed the observations of HD 332231 and produced light curves that we accessed via the TESS archive on the Mikulski Archive for Space Telescopes (MAST).⁴⁹ A single transit is present in the Sector 15 light curve produced by the SPOC presearch data conditioning (PDC) module, which removes instrumental systematics and corrects the photometric aperture for the stellar scene (e.g., Smith et al. 2012; Stumpe et al. 2012, 2014). No transits are present in the Sector 14 SPOC PDC light curve. According to the Sectors 14–15 Data Validation report for HD 332231 (Twicken et al. 2018; Li et al. 2019), the SPOC automated transit search (Jenkins et al. 2002, 2010) detected the Sector 15 transit. However, lacking a clear additional transit, the pipeline paired this event with a subtle patch of noisy data in Sector 14. As a result, this target was not classified as a SPOC TOI due to its odd–even transit depth comparison statistic. The MIT Quick Look Pipeline (Huang et al. 2018) also detected the transit in Sector 15. With additional manual vetting, this target was assigned the TOI number 1456.

The SPOC Sector 14 PDC light curve contains two data gaps in addition to the usual gap marking TESS perigee. Partially motivated by ongoing Doppler spectroscopy observations (Section 2.4), we explored the source of these data gaps. We used the `Lightkurve` package (Lightkurve Collaboration et al. 2018)⁵⁰ to decode the light-curve “bitmask” and determine that scattered light caused the two additional data gaps. We then acquired the target pixel data for HD 332231 in Sector 14 from MAST to generate light curves that included the

data contaminated by scattered light. In what follows, we describe two analyses of the Sector 14 target pixel data. The first analysis produced a “first-order” light curve that still contained certain systematic features but was sufficiently precise to search for planetary transits. This procedure serves as a useful recipe for stars with similar background contamination issues. The second analysis produced a cleaner and fully detrended light curve that we later used in our modeling.

To generate the “first-order” light curve, we isolated HD 332231 between pixel rows 683–694 and pixel columns 1659–1672 (Figure 1). The photometric aperture comprised any pixels in this array with electron fluxes greater than the overall median plus four times the standard deviation. This threshold yielded a roughly rectangular photometric aperture centered on HD 332231 consisting of 22 pixels. The background aperture comprised any pixels with electron fluxes below the overall median plus 0.001 times the standard deviation. This threshold is meant to capture all pixels with flux values on the order of the median. Figure 2 shows the average background flux as function of time in Sector 14 using this aperture. Indeed, scattered light substantially impacted the observations of HD 332231.

We then subtracted the background flux time series from the target flux time series (correcting for the difference in aperture sizes) and generated a normalized, “first-order” light curve of HD 332231 in Sector 14 (Figure 3, top panel). In determining the flux in this custom aperture, we did not correct for star field crowding. According to the TESS Input Catalog version 8 (Stassun et al. 2019), the brightest source within 100” of HD 332231 is 5.63 mag fainter in the TESS bandpass. Therefore, it contributes less than 0.6% of the flux in the photometric aperture.

A transit event is clearly present in the Sector 14 “first-order” light curve generated from the target pixel data. By removing the scattered light using a background aperture, we have uncovered this transit and ensured that it is not diluted by scattered light. This is critical since scattered light could otherwise influence the planetary radius inferred from the transit.

Having discovered an additional transit event, we re-extracted the Sector 14 light curve, experimenting with photometric apertures of different shapes and sizes, and settled on a light curve from a slightly smaller aperture than that shown in Figure 1. We used a similar strategy to measure and remove scattered background light. We removed instrumental systematics by decorrelating the light curve with the standard deviation of the spacecraft quaternion time series within each exposure (Vanderburg et al. 2019) and the median flux value from our background aperture (excluding the in-transit points from the fit). We removed any stellar variability or long-term instrumental trends by dividing a best-fit basis spline from the light curve. The middle panel of Figure 3 displays the final, flattened Sector 14 light curve of HD 332231. The standard deviation of the out-of-transit normalized flux is 585 parts per million (ppm), which we treat as the uncertainty on each data point.

The PDC light curve of HD 332231 from Sector 15 also contains masked data due to scattered light contamination. These data gaps occur near the end of each orbit and do not hide any exoplanet transits. As a result, we proceeded with the SPOC PDC light curve for Sector 15, ignoring the masked data

⁴⁹ <https://archive.stsci.edu/tess/>

⁵⁰ <https://docs.lightkurve.org/>

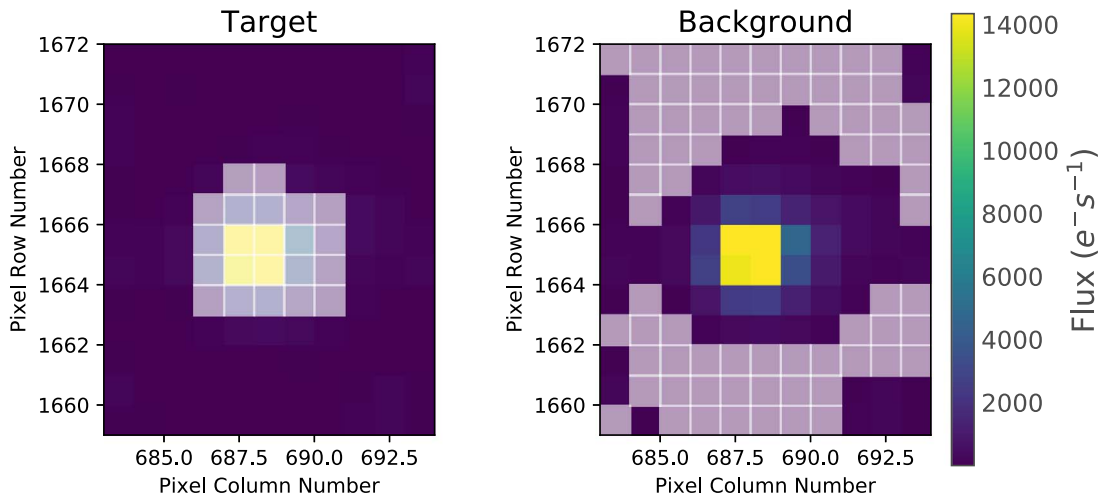


Figure 1. Apertures applied to the Sector 14 target pixel data to generate a “first-order” light curve. White boxes indicate pixels included in each aperture. Left: photometric aperture for HD 332231. Right: background aperture for the correction of scattered light.

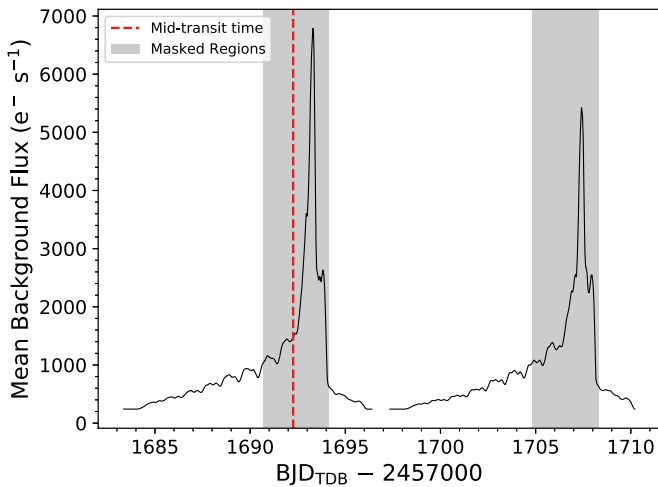


Figure 2. Mean background flux per pixel in the “first-order” background aperture for HD 332231 in Sector 14. Gray regions highlight data that were masked in the SPOC PDC light curve. The red line marks the mid-time of the transit that was initially hidden due to this masking.

(Figure 3, top panel). Any background flux, including scattered light, is removed by the photometric analysis module prior to PDC (Twicken et al. 2010). Therefore, the Sector 15 transit is not diluted. We flattened the light curve using a Savitzky–Golay filter (Savitzky & Golay 1964) with a window length of 1001 cadences to remove low-frequency noise. The middle panel of Figure 3 displays the final, flattened Sector 15 light curve of HD 332231. The standard deviation of the out-of-transit normalized flux is 547 ppm, which we treat as the uncertainty on each data point. In Figure 4, the transit events from Sectors 14 and 15 are plotted together to demonstrate the similarity in depth, duration, and shape.

2.2. Reconnaissance Spectroscopy

The TESS observations of HD 332231 motivated follow-up spectroscopy to characterize the system and explore false-positive scenarios for the transits. We acquired a single reconnaissance spectrum with the Tillinghast Reflector Echelle

Spectrograph (TRES) on the 1.5 m telescope at the Fred L. Whipple Observatory (FLWO). The spectrum has a resolution of $R = 44,000$ in the wavelength range 3850–9096 Å and a signal-to-noise ratio (S/N) of roughly 50. By visual inspection, the TRES spectrum does not contain two sets of spectral lines that would be indicative of a spectroscopic binary system. We used the Stellar Parameter Classification Tool (SPC; Buchhave et al. 2012, 2014) to extract various properties of HD 332231 from the TRES spectrum including effective temperature (T_{eff}), surface gravity ($\log g$), metallicity ($[M/H]$), and projected rotational velocity ($v \sin i$). The spectroscopic parameters inferred with SPC are listed in Table 1.

2.3. Speckle Imaging

HD 332231 was observed on the night of 2019 November 9 using the NN-explore Exoplanet Stellar Speckle Imager (NESSI; Scott et al. 2018) on the 3.5 m Wisconsin-Indiana-Yale-NOAO (WIYN) Telescope at Kitt Peak National Observatory. Sequences of diffraction-limited, 40 ms speckle exposures were taken simultaneously in the NESSI r -band and the NESSI i -band on the blue and red cameras, respectively. The image was reconstructed following the procedures outlined in Howell et al. (2011). In Figure 5, we show that we achieve magnitude contrasts of $\Delta i > 5$ and $\Delta r > 4$ at a separation of less than $0''.4$. The speckle image rules out the possibility that the transit signal observed by TESS was due to a faint stellar companion or a blended eclipsing binary.

2.4. Doppler Spectroscopy

We began monitoring the RV variation of HD 332231 in 2019 October to measure the companion’s mass and further characterize the system. The majority of the RV observations were acquired with the 2.4 m Automated Planet Finder (APF; Radovan et al. 2014; Vogt et al. 2014) Telescope at Lick Observatory under the TESS–Keck Survey (TKS) and another program dedicated to single-transit follow-up (2019B-A006, PI: Dalba). TKS is a collaboration between the University of California, the California Institute of Technology, the University of Hawaii, and NASA organized through the California Planet Search with the goal of acquiring substantial RV follow-

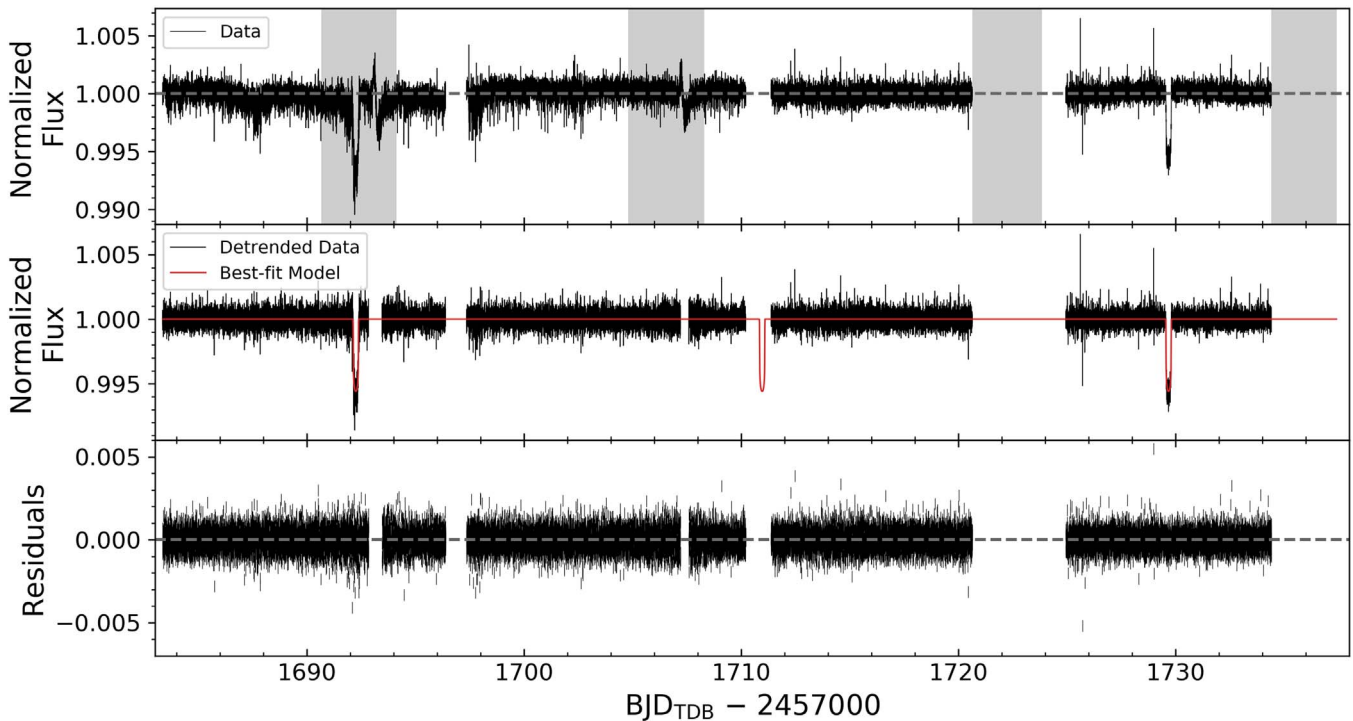


Figure 3. TESS photometry of HD 332231 from Sectors 14 and 15. Top: normalized light curves prior to detrending. This includes the “first-order” light curve from Sector 14 that was extracted from target pixel data using a custom aperture and scattered light subtraction routine (see text). The Sector 15 light curve is the SPOC PDC data product. The gray regions show the timing of the PDC data gaps from stray light masking. Middle: fully detrended light curves and the best-fit model from the global fit (see Section 3). An additional transit of HD 332231 b occurred (but was not observed) during the data gap near $\text{BJD}_{\text{TDB}} \approx 2458711$, which separates Sectors 14 and 15. Bottom: residuals between the data and best-fit model from the global fit.

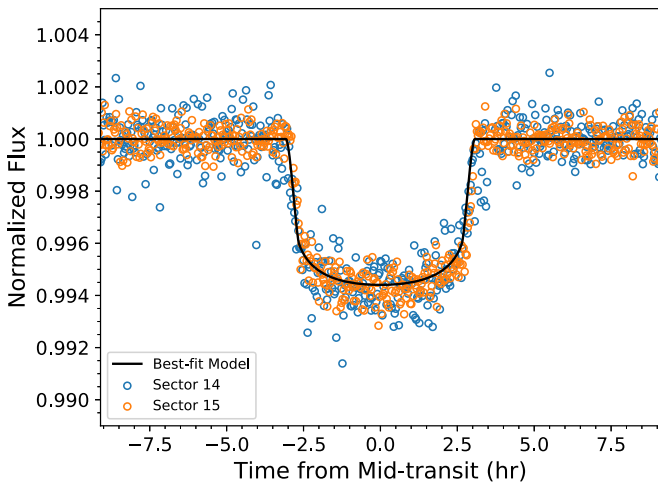


Figure 4. Transits of HD 332231 b from Sectors 14 and 15 folded on the best-fit ephemeris from the global model fit (Table 4). The best-fit transit model is also shown.

up observations for TESS. We supplemented the APF data set with additional observations from the 10 m Keck I telescope at the W. M. Keck Observatory. Here, we describe the collection and analysis of each set of RV measurements.

2.4.1. APF-Levy

The APF telescope is equipped with the Levy Spectrograph, which is a high-resolution slit-fed optical echelle spectrometer (Radovan et al. 2010). APF-Levy observed HD 332231 using the W decker, which has a width of $1''$ in the spectral dimension and $3''$ in the spatial dimension. This slit provides a resolving

Table 1
Spectroscopic Parameters for HD 332231 from TRES, Automated Planet Finder, and Keck Spectra

Property	Keck	APF	TRES
T_{eff} (K)	6100 ± 100	6070 ± 100	6130 ± 50
$\log g$ (dex)	4.3 ± 0.1	4.2 ± 0.1	4.3 ± 0.1
[Fe/H] (dex)	0.04 ± 0.06	0.05 ± 0.06	...
[M/H] (dex)	-0.01 ± 0.08
$v \sin i$ (km s^{-1})	5.3 ± 1.0	5.4 ± 1.0	7.0 ± 0.5
M_* (M_{\odot})	1.13 ± 0.05	1.13 ± 0.07	...
R_* (R_{\odot})	1.29 ± 0.03	1.4 ± 0.2	...

Note. The final spectroscopic properties that should be adopted for HD 332231 derive from the global fit to the transit and RV data (Section 3) and are listed in Table 3.

power of $R \approx 114,000$ for a continuous spectrum between 3740 and 9700 Å. A cell containing warm iodine gas placed in the light path enables the precise wavelength calibration of the observed spectra and instrument profile tracking. Additionally, we acquired a high-S/N spectrum of HD 332231 without the iodine cell which was used as a template for measuring the Doppler shifts of spectral absorption lines. During each exposure, an exposure meter monitored guider images to determine the photon-weighted mid-exposure time and when the desired precision had been reached (Kibrick et al. 2006). We extracted a relative RV from each spectrum following the forward modeling process described by Fulton et al. (2015b) and originally designed by Butler et al. (1996). Furthermore, we calculated the stellar chromospheric activity S_{HK} -index for each exposure following Isaacson & Fischer (2010). The Pearson correlation coefficient between the S_{HK} -indices and the

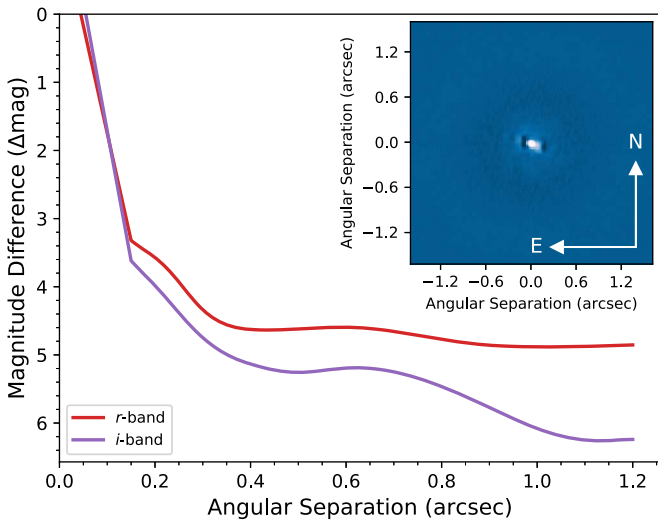


Figure 5. HD 332231 contrast curve and reconstructed *i*-band image from the NESSI speckle observations.

RV measurements is 0.032, which suggests little to no correlation between them.

For most of the APF-Levy observations, we acquired two or three successive exposures to increase signal while keeping each exposure time shorter than 20 minutes. The APF telescope is robotic and operates according to a queue that determines suitable targets based on priority and observing conditions. However, on rare occasions, HD 332231 was observed in sub-optimal conditions. We manually excluded four exposures from our analysis that were acquired during civil twilight or with seeing greater than $3''$ or that had an S/N from photon statistics below 25. In total, APF-Levy collected 68 science-quality iodine-in spectra of HD 332231 (Table 2). The time series and phase-folded RV observations of HD 332231 are shown in Figure 6.

Since the high-S/N template spectrum of HD 332231 was not observed through the iodine cell, we extracted stellar spectroscopic parameters from this spectrum following the synthetic spectral matching tool *SpecMatch* (Fulton et al. 2015a; Petigura et al. 2017). Stellar parameters output from this procedure are shown in Table 1. For parameters that were also extracted from the TRES spectrum of HD 332231 (Section 2.2), we find agreement with the APF-Levy values to better than 2σ .

While the Doppler monitoring of HD 332231 with the APF was ongoing, we modeled the RV variation and inferred planetary and orbital parameters of HD 332231 b using the *RadVel* package⁵¹ (Fulton et al. 2018). *RadVel* samples the posterior probability densities of the various model parameters using the Markov chain Monte Carlo sampler *emcee* (Foreman-Mackey et al. 2013). After the first dozen RV epochs, we began to suspect that the orbital period of HD 332231 b was short enough to have placed another transit in Sector 14. This inspired the manual analysis of target pixel level data described in Section 2.1.

2.4.2. Keck-HIRES

We supplemented the Doppler observations of HD 332231 from APF-Levy with RVs obtained at the Keck I telescope.

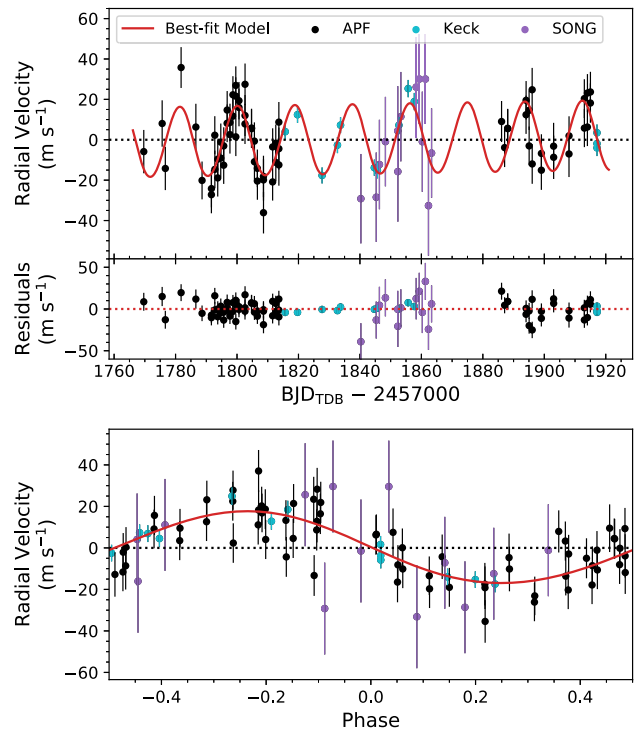


Figure 6. RV observations of HD 332231 and best-fit model described in Section 3. Top: the time-series RV observations from APF-Levy, Keck-HIRES, and SONG clearly identify a Keplerian signal due to HD 332231 b. The best-fit model includes an acceleration parameter that describes the slope of the RVs, but such a trend is not statistically preferred by the data (see Section 4.3 for a discussion). Bottom: RV observations of HD 332231 folded on the best-fit orbital ephemeris.

Table 2
RV Measurements of HD 332231

BJD _{TDB} - 2457000	RV (m s ⁻¹)	S_{HK}^a	Tel.
1769.65399	-4.6 ± 6.1	0.101 ± 0.002	APF
1775.63931	9.4 ± 7.3	0.152 ± 0.002	APF
1776.66888	-12.9 ± 6.1	0.147 ± 0.002	APF
1781.80269	37.1 ± 4.9	0.147 ± 0.002	APF
1786.60870	7.6 ± 7.4	0.121 ± 0.002	APF

Note.

^a The S_{HK} values measured by APF-Levy and Keck-HIRES have different zero-points.

(This table is available in its entirety in machine-readable form.)

Keck I is equipped with the High Resolution Echelle Spectrometer (HIRES; Vogt et al. 1994), which has a substantial record of characterizing exoplanet systems (e.g., Howard et al. 2010; Fulton et al. 2017). We acquired 13 high-resolution ($R \approx 60,000$) spectra of HD 332231. As for APF-Levy, the starlight passed through a heated iodine cell that enabled precise wavelength calibration. We also acquired a high-S/N spectral template using Keck-HIRES that was used in the forward modeling procedure to determine the relative RVs of HD 332231 (Howard et al. 2010; Howard & Fulton 2016). The Keck-HIRES RVs for HD 332231 are given in Table 2 and are shown in Figure 6. Each RV measurement from Keck-HIRES is also accompanied by an S_{HK} -index

⁵¹ <https://radvel.readthedocs.io/en/latest/>

(Isaacson & Fischer 2010). Importantly, the S_{HK} -values measured in the Keck-HIRES spectra have different zero-points than those measured in the APF-Levy spectra. They should not be directly compared. The Pearson correlation coefficient between the Keck-HIRES S_{HK} -indices and RVs is 0.29. We caution, however, that this metric is hard to interpret with so few data points. The lack of correlation between the APF S_{HK} -indices and the RVs for HD 332231 increases the confidence that the Keplerian signal is not an artifact of stellar chromospheric activity. Just as with the APF high-S/N template, we processed the Keck-HIRES template with SpecMatch. The resulting spectroscopic parameters are listed in Table 1 for comparison with similar parameters derived from APF and TRES observations. The spectroscopic parameters inferred from the spectra from each of these three sources are consistent to well within 2σ in all cases.

2.4.3. SONG Telescope

Additional RV measurements were collected using the robotic 1 m Hertzprung Stellar Observations Network Group (SONG) telescope (e.g., Andersen et al. 2014; Fredslund Andersen et al. 2019) which is equipped with a high-resolution echelle spectrograph and uses the iodine method for precise RV calibration (Grundahl et al. 2017). Thirteen spectra of HD 332231 were acquired using a slit of width $1''.24$ ($R \approx 90,000$) covering the wavelength range 4400–6900 Å. Each spectrum was obtained using an exposure time of 2700 s resulting in an S/N of ~ 50 . The RVs were determined using the iSONG pipeline (e.g., Corsaro et al. 2012; Antoci et al. 2013), which requires a high-S/N template spectrum ($R \approx 110,000$). The spectral-line-spread function of the spectrograph was determined by observing a fast rotating O star (HR 1087) through the iodine cell. Uncertainties range from 10 m s^{-1} for epochs with a high S/N to 15 m s^{-1} for those with a lower S/N. The SONG RVs are given in Table 2 and displayed in Figure 6.

3. Global Modeling

Using the EXOFASTv2 modeling suite (Eastman et al. 2013, 2019), we globally fit the available RVs from APF-Levy and Keck-HIRES with the TESS photometry to extract the full system parameters. We first conduct a fit to the archival broadband photometry with a model spectral energy distribution (SED) of HD 332231 to get a constraint on R_* . For this SED-only fit, we use the MESA Isochrones and Stellar Tracks (MIST) stellar evolution models (Paxton et al. 2011, 2013, 2015; Choi et al. 2016; Dotter 2016) and a Gaussian prior on [Fe/H] (0.04 ± 0.06 dex) from the SpecMatch analysis of the Keck-HIRES template spectrum, and on the parallax measured by Gaia (12.4498 ± 0.04404 mas), corrected for the offset reported by Stassun & Torres (2018). We also place an upper limit on the maximum line-of-extinction from the galactic reddening maps from Schlegel et al. (1998). We get a radius of $1.276 R_{\odot}$ from this analysis. We then globally fit the available RVs with the TESS photometry, and place Gaussian priors on T_{eff} (6100 ± 100 K) and [Fe/H] (0.04 ± 0.06 dex) from spectroscopy. We use the determined radius from the SED fit with a 3.5% prior as an additional Gaussian prior on the fit. We adopt this prior since interferometric radii measurements can show differences of up to $\sim 3\%$ (White et al. 2018). Within this fit, the MIST

Table 3
Median Values and 68% Confidence Intervals for Stellar Parameters in the Global Model of HD 332231

Parameter	Description (Units)	Values
M_*	Mass (M_{\odot})	1.127 ± 0.077
R_*	Radius (R_{\odot})	$1.277^{+0.039}_{-0.036}$
L_*	Luminosity (L_{\odot})	$2.02^{+0.19}_{-0.18}$
ρ_*	Density (g cm^{-3})	$0.766^{+0.061}_{-0.072}$
$\log g$	Surface gravity	$4.279^{+0.027}_{-0.034}$
T_{eff}	Effective temperature (K)	6089^{+97}_{-96}
[Fe/H]	Metallicity (dex)	$0.036^{+0.059}_{-0.058}$
[Fe/H] ₀ ^a	Initial metallicity	$0.095^{+0.055}_{-0.057}$
Age	Age (Gyr)	$4.3^{+2.5}_{-1.9}$

Note.

^a The initial metallicity is the metallicity of the star when it was formed.

isochrones are used to determine the stellar parameters in combination with the priors listed above (Table 3). The results of the fit are shown in Figures 3, 4, and 6. A set of fitted and derived planetary parameters for HD 332231 b are listed in Table 4.

4. Discussion

4.1. A Planet on the Border between Neptunian and Jovian Classes

HD 332231 b occupies an interesting area of parameter space relative to the solar system planets. By radius, HD 332231 b is 13% smaller than Jupiter and 4% larger than Saturn. Yet its mass is 19% below that of Saturn. Following the planetary class divisions of Chen & Kipping (2017), the mass of HD 332231 b places it among “Neptunian” as opposed to “Jovian” planets. Indeed, on a mass–radius diagram of well characterized planets (Figure 7), HD 332231 b resides on the edge of the cluster of giant planets whose radii are seemingly not correlated with planet mass. This makes HD 332231 b an interesting case for further exploration into the division between Neptunian and Jovian planets.

To explore the possible interior properties of HD 332231 b, we overlay contours in Figure 7 showing the core mass of giant hydrogen–helium–rich planets with 0.1 au orbits according to planetary evolution models (Fortney et al. 2007). These models suggest a core mass for HD 332231 b between 10 and $25 M_{\oplus}$, which would account for 13%–32% of its total mass. This prediction is broadly consistent with current estimates for the core masses of Jupiter (7–25 M_{\oplus} ; Wahl et al. 2017) and Saturn (5–20 M_{\oplus} ; Helled & Guillot 2013). Although 10–25 M_{\oplus} is a wide range, the planetary evolution models of Fortney et al. (2007) clearly predict that the core of HD 332231 b is unlikely to be 0 M_{\oplus} (i.e., no core).

If the core mass of HD 332231 b is similar to those of Jupiter and Saturn, then could HD 332231 b be a Jovian planet with a relatively low-mass envelope? This possibility could be explored through a measurement of the metal enrichment in the atmosphere of HD 332231 b. The atmospheres of Jupiter and Saturn are enriched in heavy elements relative to solar composition gas by factors of ~ 4 and ~ 10 , respectively (Wong et al. 2004; Fletcher et al. 2009). This enrichment relates to the accretion of planetesimals during formation, which in turn depends on when and where formation occurred, the properties of the protoplanetary disk, and the presence of companions. If

Table 4
Median Values and 68% Confidence Intervals for the Planetary Parameters in the Global Model of HD 332231

Parameter	Description (Units)	Values			
P	Period (days)	18.71204 ± 0.00043			
R_p	Radius (R_p)	$0.867^{+0.027}_{-0.025}$			
M_p	Mass (M_p)	0.244 ± 0.021			
T_C	Time of conjunction (BJD _{TDB})	$2458692.25579^{+0.00077}_{-0.00078}$			
T_0^a	Optimal conjunction Time (BJD _{TDB})	$2458729.67987 \pm 0.00038$			
a	Semimajor axis (au)	$0.1436^{+0.0032}_{-0.0033}$			
i	Inclination (degrees)	$89.68^{+0.22}_{-0.28}$			
e	Eccentricity	$0.032^{+0.030}_{-0.022}$			
ω_*	Argument of periastron (degrees)	47^{+69}_{-74}			
$e \cos \omega_*$		$0.011^{+0.028}_{-0.018}$			
$e \sin \omega_*$		$0.010^{+0.034}_{-0.019}$			
T_{eq}^b	Equilibrium temperature (K)	876 ± 17			
τ_{circ}	Tidal circularization timescale (Gyr)	630^{+110}_{-100}			
K	RV semi-amplitude (m s^{-1})	17.3 ± 1.2			
R_p/R_*	Radius of planet in stellar radii	$0.06976^{+0.00041}_{-0.00039}$			
a/R_*	Semimajor axis in stellar radii	$24.21^{+0.62}_{-0.78}$			
δ	Transit depth (fraction)	$0.004867^{+0.000058}_{-0.000055}$			
τ	Ingress/egress transit duration (days)	$0.01700^{+0.00086}_{-0.00029}$			
T_{14}	Total transit duration (days)	$0.2565^{+0.0011}_{-0.0010}$			
b	Transit impact parameter	$0.133^{+0.12}_{-0.092}$			
ρ_p	Density (g cm^{-3})	$0.464^{+0.054}_{-0.052}$			
$\log g_p$	Surface gravity	$2.905^{+0.040}_{-0.044}$			
$\langle F \rangle$	Incident flux ($10^9 \text{ erg s}^{-1} \text{ cm}^{-2}$)	$0.1335^{+0.011}_{-0.0098}$			
T_P	Time of periastron (BJD _{TDB})	$2458690.2^{+3.3}_{-3.9}$			
T_S	Time of eclipse (BJD _{TDB})	$2458701.74^{+0.34}_{-0.21}$			
T_A	Time of ascending node (BJD _{TDB})	$2458687.72^{+0.27}_{-0.16}$			
T_D	Time of descending node (BJD _{TDB})	$2458696.93^{+0.20}_{-0.21}$			
$\dot{\gamma}$	RV slope ($\text{m s}^{-1} \text{ day}^{-1}$)	0.023 ± 0.020			
Wavelength Parameters		TESS			
u_1	Linear limb-darkening coefficient	0.253 ± 0.027			
u_2	Quadratic limb-darkening coefficient	0.289 ± 0.034			
Telescope Parameters		APF	KECK	SONG	
γ_{rel}	Relative RV offset (m s^{-1})	1.3 ± 1.2	-1.9 ± 1.2	1.9 ± 6.5	
σ_J	RV jitter (m s^{-1})	$8.87^{+1.0}_{-0.92}$	$3.64^{+1.4}_{-0.99}$	$19.8^{+7.1}_{-5.2}$	

Notes. See Table 3 in Eastman et al. (2019) for the definition and explanation of the derived and fitted parameters in EXOFASTv2.

^a Minimum covariance with period.

^b Equilibrium temperature is calculated assuming zero albedo and perfect heat redistribution.

the atmosphere of HD 332231 b is not enriched in metals, this could explain the planet's relatively low mass compared to the solar system planets and could lend insight into its formation history. Alternatively, if HD 332231 b is indeed more like a Neptunian planet, as suggested by the class divisions of Chen & Kipping (2017), then we might expect greater heavy element enrichment as is seen for Uranus and Neptune (Karkoschka & Tomasko 2011; Sromovsky et al. 2011).

The bulk density of HD 332231 b is $0.464^{+0.054}_{-0.052} \text{ g cm}^{-3}$, 32% below that of Saturn. We consider whether this relatively low density is a result of planetary radius inflation. Highly irradiated exoplanets have been found to have larger radii than predicted by standard planetary evolution models, which has been attributed to several possible mechanisms (see, for instance, Fortney & Nettelmann 2010; Baraffe et al. 2014). However, empirical evidence suggests that the mechanisms causing radius inflation are not active for giant planets receiving an insolation flux (S) below $\sim 2 \times 10^8 \text{ erg s}^{-1} \text{ cm}^{-2}$

(Demory & Seager 2011). Based on the global fit (described in Section 3), we find the insolation flux of HD 332231 b to be $S = 1.34 \times 10^8 \text{ erg s}^{-1} \text{ cm}^{-2}$, slightly below the inflation boundary. In Figure 8, we place this value in the context of other known exoplanets with measured radii. Indeed, HD 332231 b occupies a region of uninflated giant planets away from the sharp upward ramp in radius. Of the known giant exoplanets with measured radii, HD 332231 b is one of the minority that receives a low enough insolation flux to be uninflated by mechanisms relating to incident radiation. On its own, this makes HD 332231 b a valuable discovery.

This argument has several caveats. First, the radius inflation boundary is largely based on radius measurements of Jovian exoplanets (Demory & Seager 2011). If this boundary contains some yet unknown dependence on planetary mass, our conclusion that HD 332231 b is not inflated may need to be revisited. However, at present, too few Saturn-mass exoplanets are known to investigate possible variations in the inflation

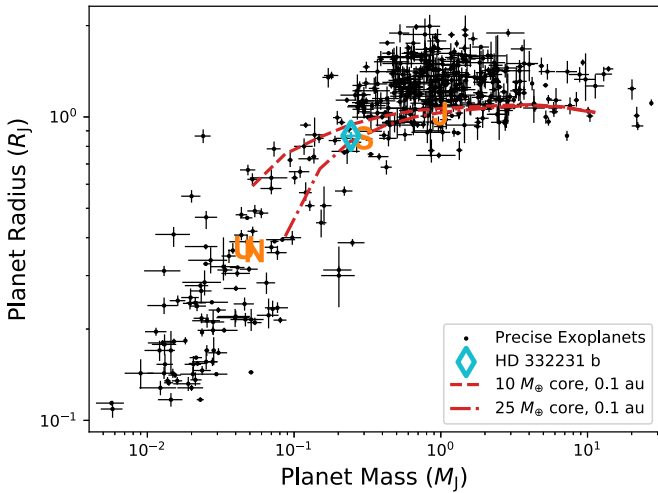


Figure 7. All known exoplanets with mass and radius measured to better than 30% precision (according to the NASA Exoplanet Archive as of 2019 December 17). The solar system’s giant planets are indicated by the letters “J,” “S,” “U,” and “N.” The dashed and dashed–dotted lines show the masses and radii of hydrogen–helium–dominated planets on 0.1 au orbits with core masses of 10 and 25 M_{\oplus} , respectively (Fortney et al. 2007). The error bars for HD 332231 b are shown but are smaller than the marker.

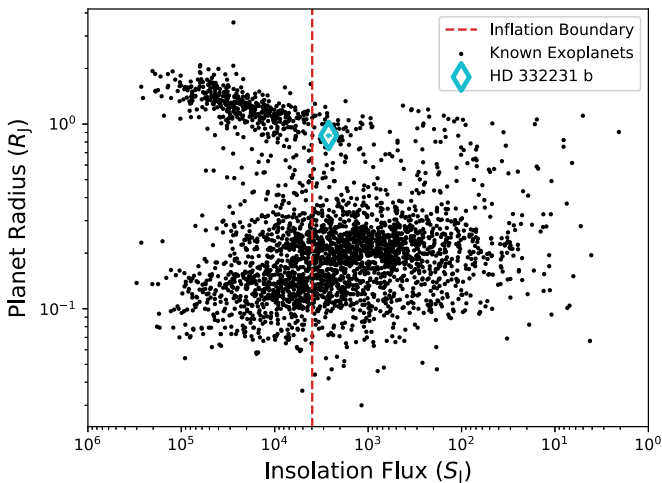


Figure 8. Planetary radius (R_p) vs. insolation flux (S) for confirmed exoplanets with the planetary and stellar parameters needed to calculate S (according to the NASA Exoplanet Archive as of 2019 December 17). The error bars for HD 332231 b are shown but are smaller than the marker. The amount of flux HD 332231 b receives is below the empirical radius inflation boundary of Demory & Seager (2011), suggesting that its radius is not inflated. HD 332231 b joins the minority of giant exoplanets with measured radii that are likely not inflated.

boundary. Second, it is possible that high-altitude aerosols or hazes could be affecting the radius of HD 332231 b (e.g., Lammer et al. 2016; Gao & Zhang 2020). This caveat could be tested through atmospheric characterization.

4.2. Atmospheric Characterization Prospects

Metal enrichment in exoplanetary atmospheres can be probed via transmission spectroscopy, for which HD 332231 b is a strong candidate. Using the properties of HD 332231 b determined in this work, we find that the transmission spectroscopy metric (TSM; Kempton et al. 2018) for HD 332231 b is $TSM = 216$. This calculation, which includes a scale factor of 1.15 for sub-Jovians, suggests that a 10 hr

observation with the Near Infrared Imager and Slitless Spectrograph on the James Webb Space Telescope would achieve an S/N of approximately 216 (Louie et al. 2018). This value readily surpasses the $TSM = 96$ recommended threshold (Kempton et al. 2018) and demonstrates that HD 332231 b is a promising target for atmospheric characterization.

Additionally, using the TSM value of HD 332231 b as a proxy for relative observability, we note that, among the planets with similar properties, HD 332231 b stands out as the most promising target. We compute the TSM value for all known transiting planets and TOIs (using the empirical mass–radius relation of Chen & Kipping 2017 as implemented in Louie et al. 2018 if masses are unknown) around late F- and early G-type stars ($5500 \text{ K} < T_{\text{eff}} < 6500 \text{ K}$) with radii $6.3 R_{\oplus} < R_p < 11.2 R_{\oplus}$ and insolation flux values 10^2 – 10^3 times that of Earth. Of planets satisfying these criteria, HD 332231 b has the highest TSM value, with the next-best being TOI 1135.01, which is one magnitude fainter in the V-band.

With an equilibrium temperature of 876 K, HD 332231 b could add dynamic range to studies of atmospheric properties as a function of temperature (e.g., Stevenson 2016) and would serve as a stepping stone between transmission spectroscopy of hot (e.g., Sing et al. 2016) and cold (Dalba et al. 2015) giant planets.

Table 4 includes the transit ephemeris of HD 332231 b measured from the TESS photometry. The precision on predictions of future transit times will degrade as time passes and future transits are not observed. From the ephemeris presented here, we estimate that the uncertainty on mid-transit time will rise to 3.0 m and 8.8 m by the years 2021 and 2030, respectively. This uncertainty is unlikely to affect future efforts to characterize the atmosphere of HD 332231 b during transit. However, since only two transits of HD 332231 b have been observed, it is not known if the ephemeris exhibits transit timing variations (TTVs). Based on the typical magnitude of TTVs in other transiting systems (Holczer et al. 2016, e.g.), it is unlikely that TTVs for HD 332231 b (if any) would preclude future in-transit atmospheric characterization (e.g., Dalba & Muirhead 2016; Dalba & Tamburo 2019). Still, the discovery of TTVs could potentially identify the existence of a companion (if any) in the HD 332231 system. For this reason, it may be useful to observe an additional transit of HD 332231 b in the near future.

4.3. Considerations of Planetary Companions and Formation History

Another possible explanation for the mass of HD 332231 b relative to its radius is the existence of a companion that reduced the amount of material in its feeding zone or truncated its growth during formation. The presence of an additional Keplerian signal (caused by a companion) is not evident in the RV time series or residuals presented in Section 2.4 (Figure 6). However, it is possible that the RV time series data show a slight linear trend that could be due to an outer companion with an orbital period much longer than the baseline of observations. We used the model comparison feature of RadVel to explore this possibility. When allowed to fit for a first-order acceleration term ($\dot{\gamma}$), RadVel converged to a solution with $\dot{\gamma} = 0.028 \pm 0.022 \text{ m s}^{-1} \text{ days}^{-1}$. We investigated the significance of this finding by comparing the Bayesian information criteria (BIC; Schwarz 1978) and the Akaike information

criteria (AIC; Akaike 1974), corrected for a small sample size (AIC_c; Sugiura 1978), for models with or without γ . The models were nearly indistinguishable from each other, having $\Delta\text{BIC} = 2.13$ and $\Delta\text{AIC}_c = 0.22$ in favor of the model without the acceleration parameter.

While the tentative trend in the RVs described by the γ parameter could have other explanations (e.g., stellar variability), it is possible that a longer RV baseline for HD 332231 could yield the discovery of a companion. RV and transit surveys have shown that the presence of outer giant planets is likely correlated to the existence of smaller inner planets (Zhu & Wu 2018; Bryan et al. 2019; Herman et al. 2019). In these studies, “smaller” typically means the inner planets are intermediate in size between the Earth and Neptune. HD 332231 b would be an interesting case if it has a companion, as it is the size of Saturn but its low mass could qualify it as a Neptunian planet (Chen & Kipping 2017).

The determination of additional planets in this system (or lack thereof) would also provide valuable context to the formation history of HD 332231 b. With an orbital period of ~ 18 days, it is unlikely that this planet experienced any tidal circularization,⁵² which all but rules out inward migration by mechanisms invoking high-eccentricity excitation. The possible existence of an outer companion may perhaps challenge this in the future. Alternatively, HD 332231 b could have migrated via interactions with its protoplanetary disk or formed in situ (Huang et al. 2016). The latter case would be supported if any small, nearby companions were to be found also transiting in the HD 332231 system. We do not find obvious evidence for transits of any such objects, although we have neither conducted an exhaustive search nor quantified our detection limits with an injection-recovery test. Therefore, HD 332231 b may demonstrate that disk migration can place giant planets on relatively short orbits.

The orbital period of HD 332231 b places it squarely in the “period valley,” which is a proposed decrease in the occurrence rate of giant planets with orbital periods between roughly 10 and 100 days (e.g., Udry et al. 2003). Different observational methods have yielded different conclusions regarding the existence and extent of the valley in period space (e.g., Udry & Santos 2007; Howard et al. 2012). However, both RV and transit surveys seem to agree that it is present between orbital periods of 10–20 days (Santerne et al. 2016; Santerne 2018). The ~ 18.7 days orbital period of HD 332231 b may then require special explanation. One possible explanation is that a companion halted the inward migration of HD 332231 b at some point either during or after its formation. This explanation has also been proposed to explain why Jupiter itself avoided a much shorter orbit during the solar system’s formation (Morbidelli & Crida 2007). Continued RV monitoring of HD 332231 can readily test this hypothesis by searching for an outer companion.

4.4. Prospects for Measuring the Stellar Obliquity

The brightness and projected rotation velocity of HD 332231 combined with the transit depth of HD 332231 b makes the system amenable to a measurement of the stellar obliquity via the Rossiter–McLaughlin (RM) effect (e.g., Winn et al. 2005). We estimate that the amplitude of the RM effect is

roughly 20 m s^{-1} assuming that $v \sin i = 6 \text{ km s}^{-1}$. The nearly central transit (i.e., impact parameter consistent with zero) may, however, challenge a spin–orbit measurement since it introduces a degeneracy into the model (Gaudi & Winn 2007). Given the timing of the RV observations and the duration of transit, it is unlikely that any of the RV measurements presented here are affected by this effect.

At the orbital separation of HD 332231 b, tidal dissipation is unlikely to have lowered the obliquity from its initial value. This means that HD 332231 b may have maintained its obliquity and may provide a window to the initial distribution of giant planet obliquities.

4.5. Scattered Light and Data Masking

Observations made by TESS in Sectors 14, 15, and 16 suffered from contamination from scattered light due to the Earth and Moon. The scattered light signal differs between each detector and even across a single detector. As described in the data release notes accompanying the TESS data,⁵³ the cadences suffering from scattered light would adversely affect the systematic error removal in the data conditioning and also the planet search. As a result, these data points were masked in the PDC light curves (Section 2.1).

Here, we briefly consider the consequence that this scattered light contamination may have on a transit search in the PDC light curves. We acquired every two-minute cadence PDC light curve from Sectors 14, 15, and 16 from MAST.⁵⁴ We scanned each light curve for quality flags that identified masked data due to scattered light. Of the combined cadences for all PDC light curves in Sector 14, 5.4% are masked due to scattered light. This fraction is 5.2% and 1.7% for Sectors 15 and 16, respectively.

The timing of the data masking is not random. As described in the TESS data release notes, the masking can result in data gaps of several days. We calculated the periodogram of the spectral window of the masked data for each of the PDC light curves in Sectors 14, 15, and 16. Peaks due to the two-minute cadence of the data were ignored. The periodogram of the spectral window of masked data for HD 332231 in Sector 14 is shown in Figure 9 as an example. In the Sector 14 light curves, the peaks in the periodogram occurred over the narrow range of 14.1313–14.1318 days, but the full width at half maximum (FWHM) power of each of these signals is 7.0–7.1 days. Unsurprisingly, this periodicity matches the orbital period of TESS around the Earth. The 7 day FWHM, however, demonstrates that all transits of exoplanets with periods in the range 10.5–17.5 days could be hidden by the masking in the PDC light curves if only observed in Sector 14. Results are similar for Sectors 15 and 16 where the masked data have periodicities of ~ 13.7 days and ~ 14.5 days and FWHM values of ~ 7.4 days and ~ 6.8 days, respectively.

Inspecting the target pixel data (as in Section 2.1) for individual Sectors 14, 15, and 16 targets is straightforward and highly advisable. However, such inspection may be more challenging for comprehensive transit searches that benefit from the processed PDC light curves. Moving forward, it may be beneficial to develop additional means of addressing scattered light contamination in PDC light curves.

⁵² The tidal circularization timescale for HD 332231 b is found to be ~ 630 Gyr (Table 4).

⁵³ https://archive.stsci.edu/tess/tess_drn.html

⁵⁴ Accessed 2019 November 21 (<https://archive.stsci.edu/tess/>).

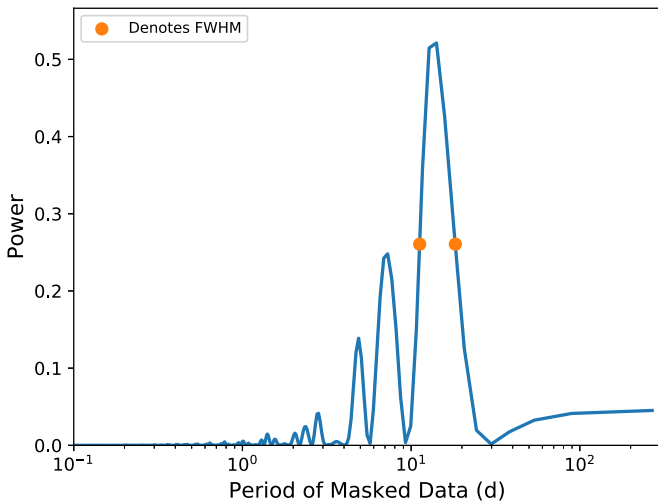


Figure 9. Periodogram of the spectral window of the masked data for HD 332231 from Sector 14. Peaks due to the data cadence are not shown. This periodogram shows a peak near 14 days with a FWHM of ~ 7 days, which is typical for stars observed in Sector 14 at two-minute cadence.

5. Conclusion

TESS observed HD 332231 (TOI 1456), an eighth magnitude F8 dwarf star, in Sectors 14 and 15 of its primary mission (Figure 3). We identified a 6.2 hr, ~ 4900 ppm single transit in the Sector 15 two-minute cadence PDC light curve of HD 332231. Subsequent spectroscopic and imaging observations from TRES (Section 2.2) and NESSI (Figure 5) ruled out common non-planetary (i.e., false-positive) scenarios for this signal. We then began follow-up radial velocity observations with the APF telescope at Lick Observatory and the Keck I telescope at W. M. Keck Observatory (Figure 6). The determination of the orbital period of the planet candidate via RV observations motivated the analysis of TESS target pixel data, which uncovered a Sector 14 transit that had previously been masked due to scattered light contamination (Figure 2). A joint analysis of the photometric and spectroscopic observations of HD 332231 confirm the existence of a Saturn-size ($0.867^{+0.027}_{-0.025} R_J$), sub-Saturn-mass ($0.244 \pm 0.021 M_J$) exoplanet, HD 332231 b.

The orbit of HD 332231 b has a period of 18.71 days and is essentially circular ($e = 0.032^{+0.030}_{-0.022}$). Its low mass relative to its size places HD 332231 b near the transition between “Neptunian” and “Jovian” regimes (Chen & Kipping 2017). We use planetary evolution models to infer possible interior properties of HD 332231 b and place it in context with other exoplanets and the solar system giant planets (Figures 7 and 8). We predict that atmospheric characterization—especially a measurement of its atmospheric metal enrichment—would be useful in characterizing HD 332231 b. The TSM (Kempton et al. 2018) for HD 332231 b is 216, which makes it a promising weakly irradiated, giant planet target.

We do not find evidence for a companion in the HD 332231 system. However, we advocate continued spectroscopic monitoring of the system in search of additional Keplerian signals in the RV time series. The presence of a companion may help to explain the properties of HD 332231 b including its existence in the proposed “period valley” (e.g., Santerne et al. 2016).

Finally, we conduct a brief investigation of the scattered light in Sectors 14–16 that suggests that transits of exoplanets

with orbital periods between 10.5 and 17.5 days could be hidden due to data masking in TESS PDC light curves.

The authors thank the anonymous referee for a helpful review of this work. P.D. gratefully acknowledges support from a National Science Foundation (NSF) Astronomy & Astrophysics Postdoctoral Fellowship under award AST-1903811. E.A.P. acknowledges the support of the Alfred P. Sloan Foundation. L.M.W. is supported by the Beatrice Watson Parrent Fellowship and NASA ADAP Grant 80NSSC19K0597. A.C. acknowledges support from the National Science Foundation through the Graduate Research Fellowship Program (DGE 1842402). D.H. acknowledges support by the National Aeronautics and Space Administration (80NSSC18K1585, 80NSSC19K0379) awarded through the TESS Guest Investigator Program. I.J.M.C. acknowledges support from the NSF through grant AST-1824644. A.B. is supported by the NSF Graduate Research Fellowship, grant No. DGE 1745301. R.A.R. is supported by the NSF Graduate Research Fellowship, grant No. DGE 1745301. C.D.D. acknowledges the support of the Hellman Family Faculty Fund, the Alfred P. Sloan Foundation, the David & Lucile Packard Foundation, and the National Aeronautics and Space Administration via the TESS Guest Investigator Program (80NSSC18K1583). R.C. is supported by a grant from the National Aeronautics and Space Administration in support of the TESS science mission. The contribution by ML was carried out within the framework of the National Centre for Competence in Research “Planets” supported by the Swiss National Science Foundation (SNSF). M.L. also acknowledges support from the Austrian Research Promotion Agency (FFG) under project 859724 “GRAPPA.” T.D. acknowledges support from MIT’s Kavli Institute as a Kavli postdoctoral fellow. D.D. acknowledges support from NASA through Caltech/JPL grant RSA-1006130 and through the TESS Guest Investigator Program Grant 80NSSC19K1727. D.J.S. is supported as an Eberly Research Fellow by the Eberly College of Science at the Pennsylvania State University. The Center for Exoplanets and Habitable Worlds is supported by the Pennsylvania State University, the Eberly College of Science, and the Pennsylvania Space Grant Consortium. H.P.O. acknowledges funding from NCCR-Planets for the CHES postdoctoral fellowship.

The authors wish to thank Bradford Holden for assistance in scheduling some of the observations presented in this paper. T. J., M.H.K., and D.L. gratefully acknowledge Allan R. Schmitt and Troy Winarski for making their light-curve software `LcTools` and `AKO-TPF` freely available.

Resources supporting this work were provided by the NASA High-End Computing (HEC) Program through the NASA Advanced Supercomputing (NAS) Division at Ames Research Center for the production of the SPOC data products.

This research has made use of the NASA Exoplanet Archive, which is operated by the California Institute of Technology, under contract with the National Aeronautics and Space Administration under the Exoplanet Exploration Program.

This research has made use of the Exoplanet Follow-up Observation Program website, which is operated by the California Institute of Technology, under contract with the National Aeronautics and Space Administration under the Exoplanet Exploration Program.

Funding for the Stellar Astrophysics Centre is provided by The Danish National Research Foundation (Grant agreement no.: DNRF106).

This paper includes data collected with the TESS mission, obtained from the MAST data archive at the Space Telescope Science Institute (STScI). Funding for the TESS mission is provided by the NASA Explorer Program. STScI is operated by the Association of Universities for Research in Astronomy, Inc., under NASA contract NAS 5-26555.

Observations in this paper made use of the NN-EXPLORE Exoplanet and Stellar Speckle Imager (NESSI). NESSI was funded by the NASA Exoplanet Exploration Program and the NASA Ames Research Center. NESSI was built at the Ames Research Center by Steve B. Howell, Nic Scott, Elliott P. Horch, and Emmett Quigley.

This paper includes observations made with the Hertzprung SONG telescope operated on the Spanish Observatorio del Teide on the island of Tenerife by the Aarhus and Copenhagen Universities and by the Instituto de Astrofísica de Canarias.

Research at the Lick Observatory is partially supported by a generous gift from Google. Some of the data presented herein were obtained at the W. M. Keck Observatory, which is operated as a scientific partnership among the California Institute of Technology, the University of California, and NASA. The Observatory was made possible by the generous financial support of the W.M. Keck Foundation.

Finally, the authors wish to recognize and acknowledge the very significant cultural role and reverence that the summit of Maunakea has always had within the indigenous Hawaiian community. We are most fortunate to have the opportunity to conduct observations from this mountain.

Facilities: Automated Planet Finder (Levy), FLWO:1.5 m (TRES), Keck:I (HIRES), SONG, TESS, WIYN (NESSI).

Software: emcee (Foreman-Mackey et al. 2013), EXOFASTv2 (Eastman 2017), Lightkurve (Lightkurve Collaboration et al. 2018), RadVel (Fulton et al. 2018), SpecMatch (Fulton et al. 2015a; Petigura et al. 2017).

ORCID iDs

Paul A. Dalba <https://orcid.org/0000-0002-4297-5506>
 Arvind F. Gupta <https://orcid.org/0000-0002-5463-9980>
 Joseph E. Rodriguez <https://orcid.org/0000-0001-8812-0565>
 Diana Dragomir <https://orcid.org/0000-0003-2313-467X>
 Chelsea X. Huang <https://orcid.org/0000-0003-0918-7484>
 Stephen R. Kane <https://orcid.org/0000-0002-7084-0529>
 Samuel N. Quinn <https://orcid.org/0000-0002-8964-8377>
 Allyson Bieryla <https://orcid.org/0000-0001-6637-5401>
 Gilbert A. Esquerdo <https://orcid.org/0000-0002-9789-5474>
 Benjamin J. Fulton <https://orcid.org/0000-0003-3504-5316>
 Nicholas Scarsdale <https://orcid.org/0000-0003-3623-7280>
 Natalie M. Batalha <https://orcid.org/0000-0002-7030-9519>
 Corey Beard <https://orcid.org/0000-0001-7708-2364>
 Aida Behmard <https://orcid.org/0000-0003-0012-9093>
 Ashley Chontos <https://orcid.org/0000-0003-1125-2564>
 Courtney D. Dressing <https://orcid.org/0000-0001-8189-0233>
 Steven Giacalone <https://orcid.org/0000-0002-8965-3969>
 Michelle L. Hill <https://orcid.org/0000-0002-0139-4756>
 Lea A. Hirsch <https://orcid.org/0000-0001-8058-7443>

Andrew W. Howard <https://orcid.org/0000-0001-8638-0320>
 Daniel Huber <https://orcid.org/0000-0001-8832-4488>
 Howard Isaacson <https://orcid.org/0000-0002-0531-1073>
 Molly Kosiarek <https://orcid.org/0000-0002-6115-4359>
 Jack Lubin <https://orcid.org/0000-0001-8342-7736>
 Andrew W. Mayo <https://orcid.org/0000-0002-7216-2135>
 Teo Mocnik <https://orcid.org/0000-0003-4603-556X>
 Joseph M. Akana Murphy <https://orcid.org/0000-0001-8898-8284>
 Erik A. Petigura <https://orcid.org/0000-0003-0967-2893>
 Paul Robertson <https://orcid.org/0000-0003-0149-9678>
 Lee J. Rosenthal <https://orcid.org/0000-0001-8391-5182>
 Arpita Roy <https://orcid.org/0000-0001-8127-5775>
 Ryan A. Rubenzahl <https://orcid.org/0000-0003-3856-3143>
 Judah Van Zandt <https://orcid.org/0000-0002-4290-6826>
 Lauren M. Weiss <https://orcid.org/0000-0002-3725-3058>
 Emil Knudstrup <https://orcid.org/0000-0001-7880-594X>
 Mads F. Andersen <https://orcid.org/0000-0002-9194-8520>
 Frank Grundahl <https://orcid.org/0000-0002-8736-1639>
 Xinyu Yao <https://orcid.org/0000-0003-4554-5592>
 Joshua Pepper <https://orcid.org/0000-0002-3827-8417>
 Steven Villanueva, Jr. <https://orcid.org/0000-0001-6213-8804>
 David R. Ciardi <https://orcid.org/0000-0002-5741-3047>
 Ryan Cloutier <https://orcid.org/0000-0001-5383-9393>
 Thomas Lee Jacobs <https://orcid.org/0000-0003-3988-3245>
 Martti H. Kristiansen <https://orcid.org/0000-0002-2607-138X>
 Daryll M. LaCourse <https://orcid.org/0000-0002-8527-2114>
 Monika Lendl <https://orcid.org/0000-0001-9699-1459>
 Hugh P. Osborn <https://orcid.org/0000-0002-4047-4724>
 Enric Palle <https://orcid.org/0000-0003-0987-1593>
 Keivan G. Stassun <https://orcid.org/0000-0002-3481-9052>
 Daniel J. Stevens <https://orcid.org/0000-0002-5951-8328>
 George R. Ricker <https://orcid.org/0000-0003-2058-6662>
 Roland Vanderspek <https://orcid.org/0000-0001-6763-6562>
 David W. Latham <https://orcid.org/0000-0001-9911-7388>
 S. Seager <https://orcid.org/0000-0002-6892-6948>
 Joshua N. Winn <https://orcid.org/0000-0002-4265-047X>
 Jon M. Jenkins <https://orcid.org/0000-0002-4715-9460>
 Douglas A. Caldwell <https://orcid.org/0000-0003-1963-9616>
 Tansu Daylan <https://orcid.org/0000-0002-6939-9211>
 William Fong <https://orcid.org/0000-0003-0241-2757>
 Robert F. Goetze <https://orcid.org/0000-0003-1748-5975>
 Mark E. Rose <https://orcid.org/0000-0003-4724-745X>
 Pamela Rowden <https://orcid.org/0000-0002-4829-7101>
 Joshua E. Schlieder <https://orcid.org/0000-0001-5347-7062>
 Jeffrey C. Smith <https://orcid.org/0000-0002-6148-7903>
 Andrew Vanderburg <https://orcid.org/0000-0001-7246-5438>

References

- Akaike, H. 1974, *ITAC*, 19, 716
 Andersen, M. F., Grundahl, F., Christensen-Dalsgaard, J., et al. 2014, *RvMxAC*, 45, 83
 Antoci, V., Handler, G., Grundahl, F., et al. 2013, *MNRAS*, 435, 1563
 Baraffe, I., Chabrier, G., Fortney, J., & Sotin, C. 2014, in *Protostars and Planets VI*, ed. H. Beuther et al. (Tucson, AZ: Univ. Arizona Press), 763

- Bryan, M. L., Knutson, H. A., Lee, E. J., et al. 2019, *AJ*, **157**, 52
- Buchhave, L. A., Bizzarro, M., Latham, D. W., et al. 2014, *Natur*, **509**, 593
- Buchhave, L. A., Latham, D. W., Johansen, A., et al. 2012, *Natur*, **486**, 375
- Butler, R. P., Marcy, G. W., Williams, E., et al. 1996, *PASP*, **108**, 500
- Chen, J., & Kipping, D. 2017, *ApJ*, **834**, 17
- Choi, J., Dotter, A., Conroy, C., et al. 2016, *ApJ*, **823**, 102
- Cooke, B. F., Pollacco, D., West, R., McCormac, J., & Wheatley, P. J. 2018, *A&A*, **619**, A175
- Corsaro, E., Grundahl, F., Leccia, S., et al. 2012, *A&A*, **537**, A9
- Dalba, P. A., & Muirhead, P. S. 2016, *ApJL*, **826**, L7
- Dalba, P. A., Muirhead, P. S., Fortney, J. J., et al. 2015, *ApJ*, **814**, 154
- Dalba, P. A., & Tamburo, P. 2019, *ApJL*, **873**, L17
- Demory, B.-O., & Seager, S. 2011, *ApJS*, **197**, 12
- Dotter, A. 2016, *ApJS*, **222**, 8
- Dragomir, D., Teske, J., Günther, M. N., et al. 2019, *ApJL*, **875**, L7
- Eastman, J., Gaudi, B. S., & Agol, E. 2013, *PASP*, **125**, 83
- Eastman, J. D., Rodriguez, J. E., Agol, E., et al. 2019, arXiv:1907.09480
- Eastman, J. 2017, EXOFASTv2: Generalized Publication-Quality Exoplanet Modeling Code, Version 2, Astrophysics Source Code Library, ascl:1710.003
- Eisner, N. L., Barragán, O., Aigrain, S., et al. 2019, arXiv:1909.09094
- Fletcher, L. N., Orton, G. S., Teanby, N. A., Irwin, P. G. J., & Bjoraker, G. L. 2009, *Icar*, **199**, 351
- Foreman-Mackey, D., Hogg, D. W., Lang, D., & Goodman, J. 2013, *PASP*, **125**, 306
- Fortney, J. J., Marley, M. S., & Barnes, J. W. 2007, *ApJ*, **659**, 1661
- Fortney, J. J., & Nettelmann, N. 2010, *SSRv*, **152**, 423
- Fredslund Andersen, M., Handberg, R., Weiss, E., et al. 2019, *PASP*, **131**, 045003
- Fulton, B. J., Collins, K. A., Gaudi, B. S., et al. 2015a, *ApJ*, **810**, 30
- Fulton, B. J., Petigura, E. A., Blunt, S., & Sinukoff, E. 2018, *PASP*, **130**, 044504
- Fulton, B. J., Petigura, E. A., Howard, A. W., et al. 2017, *AJ*, **154**, 109
- Fulton, B. J., Weiss, L. M., Sinukoff, E., et al. 2015b, *ApJ*, **805**, 175
- Gao, P., & Zhang, X. 2020, *ApJ*, **890**, 93
- Gaudi, B. S., & Winn, J. N. 2007, *ApJ*, **655**, 550
- Gill, S., Bayliss, D., Cooke, B. F., et al. 2019, *MNRAS*, **491**, 2805
- Grundahl, F., Fredslund Andersen, M., Christensen-Dalsgaard, J., et al. 2017, *ApJ*, **836**, 142
- Helled, R., & Guillot, T. 2013, *ApJ*, **767**, 113
- Herman, M. K., Zhu, W., & Wu, Y. 2019, *AJ*, **157**, 248
- Holczer, T., Mazeh, T., Nachmani, G., et al. 2016, *ApJS*, **225**, 9
- Howard, A. W., & Fulton, B. J. 2016, *PASP*, **128**, 114401
- Howard, A. W., Johnson, J. A., Marcy, G. W., et al. 2010, *ApJ*, **721**, 1467
- Howard, A. W., Marcy, G. W., Bryson, S. T., et al. 2012, *ApJS*, **201**, 15
- Howell, S. B., Everett, M. E., Sherry, W., Horch, E., & Ciardi, D. R. 2011, *AJ*, **142**, 19
- Huang, C., Wu, Y., & TriAUD, A. H. M. J. 2016, *ApJ*, **825**, 98
- Huang, C. X., Burt, J., Vanderburg, A., et al. 2018, *ApJL*, **868**, L39
- Huber, D., Chaplin, W. J., Chontos, A., et al. 2019, *AJ*, **157**, 245
- Isaacson, H., & Fischer, D. 2010, *ApJ*, **725**, 875
- Jenkins, J. M., Caldwell, D. A., & Borucki, W. J. 2002, *ApJ*, **564**, 495
- Jenkins, J. M., Chandrasekaran, H., McCauliff, S. D., et al. 2010, *Proc. SPIE*, **7740**, 77400D
- Jenkins, J. M., Twicken, J. D., McCauliff, S., et al. 2016, *Proc. SPIE*, **9913**, 99133E
- Jones, M. I., Brahm, R., Espinoza, N., et al. 2019, *A&A*, **625**, A16
- Karkoschka, E., & Tomasko, M. G. 2011, *Icar*, **211**, 780
- Kempton, E. M. R., Bean, J. L., Louie, D. R., et al. 2018, *PASP*, **130**, 114401
- Kibrick, R. I., Clarke, D. A., Deich, W. T. S., & Tucker, D. 2006, *Proc. SPIE*, **6274**, 62741U
- Kovács, G., Zucker, S., & Mazeh, T. 2002, *A&A*, **391**, 369
- Lammer, H., Erkaev, N. V., Fossati, L., et al. 2016, *MNRAS*, **461**, L62
- Lendl, M., Bouchy, F., Gill, S., et al. 2020, *MNRAS*, **492**, 1761
- Li, J., Tenenbaum, P., Twicken, J. D., et al. 2019, *PASP*, **131**, 024506
- Lightkurve Collaboration, Cardoso, J. V. D. M., & Hedges, C. 2018, Lightkurve: Kepler and TESS time Series Analysis in Python, Astrophysics Source Code Library, ascl:1812.013
- Louie, D. R., Deming, D., Albert, L., et al. 2018, *PASP*, **130**, 044401
- Morbidelli, A., & Crida, A. 2007, *Icar*, **191**, 158
- Paxton, B., Bildsten, L., Dotter, A., et al. 2011, *ApJS*, **192**, 3
- Paxton, B., Cantiello, M., Arras, P., et al. 2013, *ApJS*, **208**, 4
- Paxton, B., Marchant, P., Schwab, J., et al. 2015, *ApJS*, **220**, 15
- Petigura, E. A., Howard, A. W., Marcy, G. W., et al. 2017, *AJ*, **154**, 107
- Radovan, M. V., Cabak, G. F., Laiterman, L. H., Lockwood, C. T., & Vogt, S. S. 2010, *Proc. SPIE*, **7735**, 77354K
- Radovan, M. V., Lanclus, K., Holden, B. P., et al. 2014, *Proc. SPIE*, **9145**, 91452B
- Rodriguez, J. E., Quinn, S. N., Huang, C. X., et al. 2019, *AJ*, **157**, 191
- Santerne, A. 2018, in Handbook of Exoplanets, ed. H. Deeg & J. Belmonte (Cham: Springer), 154
- Santerne, A., Moutou, C., Tsantaki, M., et al. 2016, *A&A*, **587**, A64
- Savitzky, A., & Golay, M. J. E. 1964, *AnaCh*, **36**, 1627
- Schlegel, D. J., Finkbeiner, D. P., & Davis, M. 1998, *ApJ*, **500**, 525
- Schwarz, G. 1978, *AnSta*, **6**, 461
- Scott, N. J., Howell, S. B., Horch, E. P., & Everett, M. E. 2018, *PASP*, **130**, 054502
- Sing, D. K., Fortney, J. J., Nikolov, N., et al. 2016, *Natur*, **529**, 59
- Smith, J. C., Stumpe, M. C., Van Cleve, J. E., et al. 2012, *PASP*, **124**, 1000
- Sromovsky, L. A., Fry, P. M., & Kim, J. H. 2011, *Icar*, **215**, 292
- Stassun, K. G., Oelkers, R. J., Paegert, M., et al. 2019, *AJ*, **158**, 138
- Stassun, K. G., & Torres, G. 2018, *ApJ*, **862**, 61
- Stevenson, K. B. 2016, *ApJL*, **817**, L16
- Stumpe, M. C., Smith, J. C., Catanzarite, J. H., et al. 2014, *PASP*, **126**, 100
- Stumpe, M. C., Smith, J. C., Van Cleve, J. E., et al. 2012, *PASP*, **124**, 985
- Sugiura, N. 1978, *Commun. in Statist Theory*, **A7**, 13
- Sullivan, P. W., Winn, J. N., Berta-Thompson, Z. K., et al. 2015, *ApJ*, **809**, 77
- Twicken, J. D., Catanzarite, J. H., Clarke, B. D., et al. 2018, *PASP*, **130**, 064502
- Twicken, J. D., Clarke, B. D., Bryson, S. T., et al. 2010, *Proc. SPIE*, **7740**, 774023
- Twicken, J. D., Jenkins, J. M., Seader, S. E., et al. 2016, *AJ*, **152**, 158
- Udry, S., Mayor, M., & Santos, N. C. 2003, *A&A*, **407**, 369
- Udry, S., & Santos, N. C. 2007, *ARA&A*, **45**, 397
- Vanderburg, A., Huang, C. X., Rodriguez, J. E., et al. 2019, *ApJL*, **881**, L19
- Villanueva, S., Dragomir, D., J., Gaudi, B. S., et al. 2019, *AJ*, **157**, 84
- Vogt, S. S., Allen, S. L., Bigelow, B. C., et al. 1994, *Proc. SPIE*, **2198**, 362
- Vogt, S. S., Radovan, M., Kibrick, R., et al. 2014, *PASP*, **126**, 359
- Wahl, S. M., Hubbard, W. B., Militzer, B., et al. 2017, *GeoRL*, **44**, 4649
- Wang, S., Jones, M., Shporer, A., et al. 2019, *AJ*, **157**, 51
- White, T. R., Huber, D., Mann, A. W., et al. 2018, *MNRAS*, **477**, 4403
- Winn, J. N., Noyes, R. W., Holman, M. J., et al. 2005, *ApJ*, **631**, 1215
- Winters, J. G., Medina, A. A., Irwin, J. M., et al. 2019, *AJ*, **158**, 152
- Wong, M. H., Mahaffy, P. R., Atreya, S. K., Niemann, H. B., & Owen, T. C. 2004, *Icar*, **171**, 153
- Zhu, W., & Wu, Y. 2018, *AJ*, **156**, 92